Fire Technology, 53, 1795–1832, 2017
© 2017 Springer Science + Business Media New York.
Manufactured in The United States
DOI: 10.1007/s10694-017-0657-z

Examination of WFDS in Modeling Spreading Fires in a Furniture Calorimeter

Y. Perez-Ramirez, P. A. Santoni, J. B. Tramoni and F. Bosseur, SPE–UMR 6134 CNRS, University of Corsica, Campus Grimaldi, BP 52, 20250 Corte, France*

W. E. Mell, Pacific Wildland Fire Science Laboratory, U.S. Forest Service, 400 N 34th Street, Suite 201, Seattle, WA 98103, USA

Received: 4 November 2016/**Accepted:** 19 April 2017

Abstract. Validation of physics-based models of fire behavior requires comparing systematically and objectively simulated results and experimental observations in different scenarios, conditions and scales. Heat Release Rate (HRR) is a key parameter for understanding combustion processes in vegetation fires and a main output data of physics-based models. This paper addresses the validation of the Wildland-urban interface Fire Dynamics Simulator (WFDS) through the comparison of predicted and measured values of HRR from spreading fires in a furniture calorimeter. Experimental fuel beds were made up of *Pinus pinaster* needles and three different fuel loadings (i.e. 0.6, 0.9 and 1.2 kg/m^2) were tested under no-slope and up-slope conditions (20°). An Arrhenius type model for solid-phase degradation including char oxidation was implemented in WFDS. To ensure the same experimental and numerical conditions, sensitivity analyses were carried out in order to determine the grid resolution to capture the flow dynamics within the hood of the experimental device and to assess the grid resolution's influence on the outputs of the model. The comparison of experimental and predicted HRR values showed that WFDS calculates accurately the mean HRR values during the steady-state of fire propagation. It also reproduces correctly the duration of the flaming combustion phase, which is directly tied to the fire rate of spread.

Keywords: Physics-based modeling, Numerical simulation, Solid-phase degradation, Heat released rate, Oxygen consumption calorimetry, Wildland fires

List of symbols

A	Pre-exponential factor Arrhenius rate equations
c_p	Specific heat
dx_b	Grid size in the fuel bed
$dx_{b,\delta_R/3}$	Grid size in the fuel bed computed as a third of the extinction length
$dx_{b,\delta_R/5}$	Grid size in the fuel bed computed as a fifth of the extinction length
dx_g	Grid size for the reacting flow
$dx_{g,z_c min}$	Grid size for the reacting flow computed as a sixteenth of $z_{c,line}$
$dx_{g,z_c max}$	Grid size for the reacting flow computed as a fourth of $z_{c,line}$

* Correspondence should be addressed to: Y. Perez-Ramirez, E-mail: perez-ramirez@univ-corse.fr

E	Heat released per unit mass of O_2 consumed during combustion or activation energy in Arrhenius rate equations divided by the gas constant
F_{C_D}	Drag coefficient factor
g	Standard gravity
h_b	Fuel bed depth
$h_{c,e}$	Convective heat transfer coefficient
HRR	Heat released rate
I_b	Blackbody radiation intensity
LSHR	Large Scale Hate Release apparatus (furniture calorimeter)
M	Fuel moisture content of vegetation (dry basis)
MLR	Mass loss rate
$\dot{n}^{\circ}_{O_2}$	Molar flow rate of O_2 in the incoming air
$\dot{n}_{O_2}$	Molar flow rate of O_2 in the exhaust duct
OCC	Oxygen consumption calorimetry
$\dot{q}$	Heat release rate of the fire
$\dot{q}'$	Fire line intensity
$\dot{q}'''_{c,b}$	Convective heat source
$\dot{q}''_{r,b}$	Radiative heat source
r	Radius
R	Reaction rate
Re	Reynolds number
RH	Relative humidity
std	Standard deviation
T	Temperature
$\boldsymbol{u}$	Velocity vector
U	Integrated radiation intensity
V	Volume
Veg	Vegetation
W_{O_2}	Molecular weight of O_2
Y	Mass fraction
z_c	Characteristic diameter of a fire defined by means of the heat release rate
$z_{c,line}$	Characteristic length scale of a line fire defined by means of the fire line intensity

Greek symbols

α_{char}	Fraction of the energy produced by the char combustion reaction that is deposited in the solid phase
α_e	Volume fraction of the solid-phase
β_{char}	Constant in char oxidation rate equation
β_e	Packing ratio
δ_R	Extinction length
κ	Radiative absorption coefficient
Δh_c	Mass-based heat of combustion
Δh_{char}	Heat of char oxidation
Δh_{pyr}	Heat of pyrolysis
Δh_{vap}	Heat of vaporization
μ	Dynamic viscosity of the gaseous mixture
$\nu_{O_2,char}$	Stoichiometric constant for char oxidation
ρ	Mass density
σ_e	Surface-to-volume ratio for fuel elements
χ_{ash}	Fraction of char converted to ash
χ_{char}	Fraction of the dry vegetation converted to char

χ_r	Fraction of local chemical heat release radiated to surroundings
χ_s	Fraction of consumed fuel mass converted to soot

Subscripts

a	Ambient
ash	Ash residue from combustion
b	Bulk quantity
$char$	Char oxidation
CO_2	Carbon dioxide
dry	Dry vegetation
e	Fuel element type
F	Fuel vapor
g	Gaseous mixture or gas-phase
H_2O	Water vapor
O_2	Oxygen
pyr	Pyrolysis

1. Introduction

Wildland fires are extremely complex phenomena involving processes covering a large range of scales over space and time [1]. Physics-based models attempt to represent all the processes characterizing fire behavior (e.g. from pyrolysis/ignition to smoke transport). However, they do have to employ some approximations to account for processes that occur at length scales below those explicitly resolved. Validation studies aim to characterize the impacts of these approximations and to verify that model outcomes represent the processes they aim to describe within acceptable error bounds by comparing systematically and objectively simulated results and experimental observations in different scenarios, conditions and scales [2].

Heat Release Rate (HRR; kW), the rate at which fire releases energy, is a main output data of physics-based models and it is commonly accepted as one of the most important parameters in characterizing fires [3]. HRR can provide information on fire risk and potential damage, as well as on the fire suppression opportunities. HRR can thus be used to evaluate the effects of fuel treatments on fire behavior [4], to establish limits and conditions for prescribed burning [5], or to assess fire impacts on ecosystems [6].

HRR is not a fundamental property of vegetation, but is strongly dependent on the combustion processes. Combustion of vegetation is described, in a general way, as following three stages: pre-heating, flaming combustion and glowing/smoldering combustion. So, when vegetation is exposed to a heat source, it thermally decomposes into water vapor, volatile gases and reactive char. Volatile gases are oxidized emitting heat, visible light and the flame; char undergoes heterogeneous solid–gas phase oxidation reactions, which are highly exothermic.

The accurate prediction of the production of combustible gases from vegetation and the subsequent char oxidation, which depends on the modeling of thermal degradation of vegetation, is of primary importance to predict reliable

values of mass loss rate (MLR; kg/s) and HRR. Even though the behavior of a fire results from the interaction of all the combustion stages, which do not occur uniformly or sequentially but are intrinsically linked by chemical and thermal feedbacks [7], char oxidation has not always been considered when modeling forest fires based on the assumption that flaming combustion is predominant at the head of the fire.

This work examines the capabilities of a particular physics-based model, the Wildland-urban interface Fire Dynamics Simulator (WFDS) [8, 9] to predict the HRR from flaming and char oxidation of spreading fires in a furniture calorimeter. To this purpose, fire spread experiments have been conducted in a furniture calorimeter: the Large Scale Heat Release apparatus (LSHR). Experimental fuel beds were made up of *Pinus pinaster* needles. This natural species is representative of the vegetation in the Mediterranean Basin and is frequently subjected to wildland fires. Three different fuel loadings (i.e. 0.6, 0.9 and 1.2 kg/m^2) have been tested under no-slope and up-slope conditions (20°). HRR measurements have been compared to the predictions of WFDS. In order to take into account char oxidation, an Arrhenius type model for solid degradation has been implemented in WFDS.

Experiments were carried out at laboratory scale for several reasons. On the one hand, laboratory experimentation allows for the production of well characterized data due to repeatable procedures and controlled conditions. On the other hand, laboratory environment offers the possibility to accurately measure a larger number of parameters related to fire behavior such as geometrical fire descriptors (flame height, flame depth, fire front shape) and thermodynamic quantities (HRR, MLR, heat fluxes, species yields). And last, but not least, the fact that there is no direct measurement instrument to evaluate HRR at field scale. HRR is estimated indirectly by means of the measurement of other quantities such as the rate of spread and the fuel consumed per unit area [10]. Therefore, there is an important uncertainty when comparing experimental and predicted HRR at field scale, which can result in misleading conclusions. At the laboratory-scale, oxygen consumption calorimetry (OCC) constitutes an accurate and reliable method to measure HRR [11].

The same experimental and numerical conditions must be ensured in order to compare observed and simulated data. The LSHR includes a hood extraction system which collects the gases released from the combustion processes and are used to measure the oxygen consumption and thus determine the instantaneous HRR by means of OCC. In order to assess how well the numerical model simulates the hood extraction system, and thus the flow it induces, a sensitivity analysis has been performed. Numerical results have been compared to measurements conducted with a hot wire anemometer. From this study, the grid resolution to capture the flow dynamics within the hood has been established.

Moreover, a sensitivity analysis concerning the mesh resolution within the combustion area has been conducted. In this part of the domain, the mesh size has been first estimated based on the extinction length and the experimental HRR. Then different mesh sizes have been tested to reach a compromise between the

simulation time and the accuracy of the results, and a relatively non-grid dependent solution.

The following section describes the experimental methodologies and the experiments conducted at the LSHR. Next, an overview of WFDS and the solid-phase thermal degradation model is provided. This is followed by the sensitivity analyses concerning the grid resolution to be used to capture, respectively, the flow patterns within the hood and the reacting flow dynamics as well as the radiation heat transfer in the fuel bed. After that, experimental results and numerical predictions are compared. Finally, a summary and conclusions on the capabilities of WFDS to predict spreading fires at laboratory scale and the future work are presented.

2. Experimental Methods

2.1. Fire spread Experiments

The fire spread experiments were conducted by using a 1 MW furniture calorimeter (LSHR). Fire tests were performed on a 2 m long and 2 m wide combustion bench located on a load cell (sampling rate 1 Hz and 1 g accuracy) and under a 3 m × 3 m hood with a 1 m^3/s extraction system. The experiments consisted of igniting along the 1 m edge of the rectangular porous fuel beds of 1 m width and 2 m long in order to observe the flame front spread under both no-slope conditions (Figure 1a) and up-slope conditions (20°) (Figure 1b).

(a) (b)

Figure 1. Fire spread experiments. (a) No-slope test front perspective image (b) Up-slope test side image.

Porous fuel beds were made up of pine needles (*Pinus pinaster*), spread as evenly as possible in order to obtain homogeneous fuel beds. Different fuel loadings were tested: 0.6, 0.9 and 1.2 kg/m^2. The needles were oven dried at 60°C for 24 h before the experiments. The resulting fuel moisture content was around 5% in most of the cases. However, it varied between 3% and 8%. To ensure a fast and linear ignition, a small amount of ethanol and a flame torch were used. At least four replications were carried out for each fuel loading and each inclination of the bench (0° and 20° slope). Ambient conditions were measured just before the ignition. Combustions gases (CO, CO_2) and O_2 were analyzed in the exhaust pipe. A bidirectional probe measured the exhaust gas velocity. Smoke properties in terms of extinction coefficient were also analyzed. Table 1 summarizes the main characteristics of the fuel bed configurations for each experimental case.

HRR was determined from OCC following the formulation derived by Parker [12] which is based on the measurement of the exhaust flow velocity and the gas volume fractions. Several assumptions were taken into account to perform HRR calculations. Firstly, the combustion of pine needles was represented by the stoichiometric reaction for the complete combustion of lignocellulosic materials given by the following reaction where the coefficients corresponding to the elemental composition of pine needles ($C_xH_yO_z$) were obtained from an ultimate analysis. This assumption was based on the fact that experiments were conducted under well-ventilated conditions, and it was confirmed by the weak production of carbon monoxide [10].

$$C_{4.41}H_{6.34}O_{2.44} + 4.775(O_2 + 3.76N_2) \rightarrow 4.41CO_2 + 3.17H_2O + 17.954N_2 \quad (1)$$

Secondly, all the gases were considered to behave as ideal gases. In addition, the analyzed air was defined by its composition in terms of O_2, CO_2, H_2O and N_2. All other gases were lumped into N_2. Finally, the heat release rate was computed assuming a constant amount of energy released per unit mass of oxygen consumed:

$$HRR = E\left(\dot{n}^{\circ}_{O_2} - \dot{n}_{O_2}\right)W_{O_2} \quad (2)$$

Table 1
Fuel Beds Configuration

Experimental case	Fuel loading—dry basis (kg/m^2)	Slope configuration (°)	Fuel bed mean depth (cm)
1_0	0.6	0	3.5
2_0	0.9	0	5.5
3_0	1.2	0	6.5
1_20	0.6	20	3.5
2_20	0.9	20	5.5
3_20	1.2	20	7.5

where E is the heat released per unit mass of O_2 consumed in the reaction (E = 13.98 MJ/kg, [10]), $\dot{n}^{\circ}_{O_2}$ the molar flow rate of O_2 in the incoming air, $\dot{n}_{O_2}$ the molar flow rate of O_2 in the exhaust duct and W_{O_2} the molecular weight of O_2. More details on the HRR calculation procedure can be found at Santoni et al. [11]. It is worth noting that throughout the experiments we observed the presence of both flaming and char combustion simultaneously, except during the ignition and the extinction phases. Thus, the instantaneous measures of HRR obtained by OCC correspond to the contribution of both gas and solid phase reactions.

During these experiments other important parameters describing fire behavior such as the flame height, the rate of spread, or the radiant heat flux were measured. Detailed methodologies and results can be found at [10] and [13].

2.2. *Airflow Velocity Measurements*

Measurements of airflow velocities within the hood were performed by using a hot wire anemometer (sampling rate of 50 Hz and accuracy of 0.001 m/s). Measurements were taken at different heights and for two different positions (Figure 2a), the center of the bench (position C) and 0.5 m offset from the center following the longitudinal axis of the bench (position A). At each position, A and C, measurements were performed every 10 cm covering a height from 0.2 m to 1.5 m above the bench surface. The probe sensor was placed parallel to bench surface in order to capture predominantly velocities following z-axis, which correspond to the velocity components induced by the hood extraction system. In this regard, the anemometer used is able to measure flow velocities which are perpendicular to the probe sensor and whose velocity vector stays within a cone of ±30° with respect to the probe axis (Figure 2b). Velocities at each position and height were recorded during 5 min and time average values were then computed over the whole measuring time interval. The hood extraction system was turned on several minutes before performing the measurements in order to assure a fully developed flow

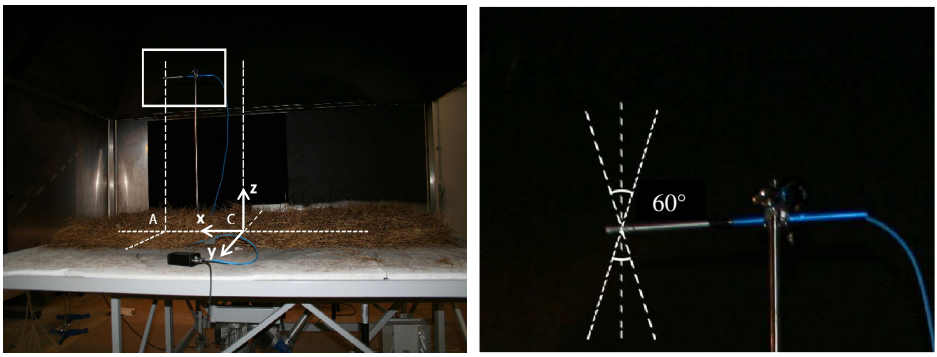

(a) (b)

Figure 2. Measurements of flow velocities. (a) Measurement positions. (b) Probe setting.

regime. Moreover, a fuel bed corresponding to a fuel loading of 0.9 kg/m^2 was present in order to take into account the effect of surface roughness on fluid flow.

3. Numerical and Modeling Approach

3.1. Overview of WFDS

WFDS is a physics-based model that attempts to comprehensively capture, within the constraints imposed by the resolution of the computational grid, the physical processes governing fire behavior in vegetation. Details of the modeling approach have been provided in Mell et al. [9]. The WFDS model, developed by the U.S. Forest Service, is largely based on the Fire Dynamics Simulator (FDS), which simulates fires in buildings and has been developed by the National Institute of Standards and Technology in the U.S. [14]. The numerical methods of computational fluid dynamics and large eddy simulation (LES) are employed to solve equations governing the conservation of momentum, total mass, and energy in the gas phase. The model equations for the thermal degradation of the vegetation, which are discussed in the next section, are coupled to the gas phase equations through heat (radiation and conduction) and mass (e.g., generation of water and fuel vapor) transfer. In the implementation of WFDS used in this study we use a thermal degradation scheme that is Arrhenius based and includes char oxidation. This differs from the thermal degradation used previously in WFDS simulations of fire spread in grassland fuels [8] and Douglas fir [9] in which a simpler approach, without char oxidation and not based on Arrhenius kinetics, was used. For the experimental scenario considered here, with relatively high bulk density fuel beds, the modeling of char oxidation is necessary in order to reproduce the measured total heat release rate from oxygen consumption calorimetry, as is discussed in the results section.

To-date, WFDS validation studies are limited in number and include both laboratory [9, 15–17] and field [8, 18–20] scenarios.

3.2. Solid-phase thermal degradation model

In this section, we provide the details for obtaining the bulk mass source terms $\left\langle \dot{m}'''_{b,i} \right\rangle_{\mathrm{Vb}}$ for water vapor ($i = \mathrm{H_2O}$), fuel vapor ($i = \mathrm{F}$) and carbon dioxide ($i = \mathrm{CO_2}$) required in the gas-phase mass, species, and energy transport equations. The model for the thermal degradation of a thermally-thin vegetative fuel used here is similar to that employed by others (e.g. [21–23]). The solid-phase thermal degradation process has three components:

1. Endothermic drying

$$\text{Virgin Veg} \rightarrow M\mathrm{H_2O} + (1 - M)\text{Dry Veg}$$

2. Endothermic pyrolysis

$$\text{Dry Veg} \rightarrow \chi_{char}\text{Char} + (1 - \chi_{char})(\text{Fuel Gas} + \text{Soot})$$

3. Exothermic char oxidation

$$Char + v_{O_2,\text{char}}O_2 \rightarrow \left(1 + v_{O_2,\text{char}} - \chi_{ash}\right)CO_2 + \chi_{ash}\text{Ash}$$

The stoichiometric constants are: M = fuel moisture mass fraction on a dry weight basis; χ_{char} mass fraction of dry fuel that is converted to char during pyrolysis; $v_{O_2,\text{char}}$ 1.65 [21]; χ_{ash} mass fraction of char that is converted to ash during char oxidation.

In the equations that follow, the subscript b denotes bulk quantities that are resolved on the computational grid. For example, the mass of dry vegetation, resolved on the computational grid, is denoted $\rho_{b,\text{dry}}$ (kg m^{-3}). In the notation of Mell et al. [9], $\rho_{b,\text{dry}} = \left\langle m'''_{\text{dry}} \right\rangle_{Vb}$, where the angled brackets denote the explicit LES filtering.

The Arrhenius rate equations for drying, pyrolysis, and char oxidation are:

$$R_{H_2O} = \rho_{b,H_2O} A_{H_2O} T_e^{-\frac{1}{2}} e^{-\frac{E_{H_2O}}{T_e}} \tag{3}$$

$$R_{pyr} = \rho_{b,\text{dry}} A_{pyr} e^{-\frac{E_{pyr}}{T_e}} \tag{4}$$

$$R_{\text{char}} = \frac{A_{\text{char}}}{v_{O_2,\text{char}}} \rho_g Y_{O_2} \sigma_e \beta_e e^{-\frac{E_{\text{char}}}{T_e}} \left(1 + \beta_{char}\sqrt{Re_e}\right) \tag{5}$$

Table 2
Solid Phase Parameters Used in the Thermal Degradation Model

Symbol (units)	Value	Comments
M (−)	See Table 3	
χ_{char} (−)	See Table 3	
χ_{ash} (−)	See Table 3	
Δh_{vap} (kJ/kg)	2259	[21]
A_{H_2O} ($\sqrt{K}$/s)	600,000	[21]
E_{H_2O} (K)	5800	[21]
Δh_{pyr} (kJ/kg)	418	[21]
A_{pyr} (1/s)	36,300	[21]
E_{pyr} (K)	7250	[21]
Δh_{char} (kJ/kg)	−32,740	[24]
A_{char} (m/s)	215	Empirically determined in this study
E_{char} (K)	9000	[21]
$v_{O_2,char}$	1.65	[21]
β_{char}	0.2	[21]

The values of the kinetic constants are given in Table 2.The Reynolds number is $Re_e = 2\rho_g|\mathbf{u}|r_e/\mu$ ith $r_e = 2/\sigma_e$ The term containing Re_e is included to account for the oxygen blowing effects on char oxidation and the constant β_{char} is equal to 0.2 by default, which is the value used by Porterie et al. [21].

The equation governing the temperature, T_e of the thermally thin fuel elements in a gas phase computational grid cell of volume V_b is

$$\rho_b c_{p,e}\frac{dT_e}{dt} = -\Delta h_{vap}R_{H_2O} - \Delta h_{pyr}R_{pyr} - \alpha_{char}\Delta h_{char}R_{char} - \left\langle \dot{q}'''_{c,b}\right\rangle_{Vb} - \left\langle \nabla\cdot\dot{\mathbf{q}}''_{r,b}\right\rangle_{V_b} \tag{6}$$

The first three terms on the right-hand-side are, respectively, endothermic drying, endothermic pyrolysis, exothermic char oxidation. The non-dimensional weighting parameter, α_{char} is the fraction of the heat generated by heterogeneous char oxidation that is deposited in the fuel element and $(1-\alpha_{char})$ in the gas phase. Here $\alpha_{char} = 0.5$, which has been used by others (e.g., Porterie et al. [21]). The fourth and fifth terms on the right-hand-side of Equation (6) are the fuel element bulk contributions of convective and radiative heat transfer, respectively [9]. The heats in Equation (6) are $\Delta h_{vap} = 2.259 \times 10^3$ J kg^{-1}; $\Delta h_{pyr} = 418$ J kg^{-1} [21]; Δh_{char} -32×10^3 J kg^{-1} [24].

The modeling of the net convective and radiative heat transfer to the vegetation in the LES approach implemented in WFDS was described in detail in [9]. A short overview follows. The convective heat transfer term in Equation (6) is

$$\left\langle \dot{q}'''_{c,b}\right\rangle_{Vb} = \beta_e\sigma_e h_{c,e}\left(T_e - T_g\right) \tag{7}$$

where $\langle(\ )\rangle$ denotes the explicit box filter of the LES method [9], β_e and σ_e (m^{-1}) are the packing ratio and surface-to-volume ratio of vegetation of type e; T_g is the temperature in the gas-phase and the convective heat transfer coefficient $h_{c,e}$ (W m^{-2} s^{-1}) (Porterie et al., [25]) is

$$h_{c,e} = 0.5k\left(T_g\right)\frac{0.683Re_e^{0.687}}{2/\sigma_e} \tag{8}$$

with Re_e represents the Reynolds number as previously described. The radiation heat transfer term in Equation (6) is

$$\left\langle \nabla\cdot\dot{q}''_{r,b}\right\rangle_{Vb} = \kappa_{b,e}[4\pi I_b(T_e) - U] \tag{9}$$

where $\kappa_{b,e} = \sigma_e\beta_e/4$ (m^{-1}) is the radiation absorption coefficient due the subgrid vegetation, and U (W m^{-2}) is the integrated radiation intensity.

The gray gas form of the three-dimensional radiation transfer equation is solved using a finite volume method. Capturing the effects of subgrid heterogeneity of the flame temperature requires special treatment of the radiation emission term since

it depends on the fourth power of the local temperature. In regions where the local meaning temperature is lower and the spatial gradients of scalars are sufficiently resolved, capturing the effects of the subgrid temperature distribution is less critical. For this reason, we model the gas phase emission term as follows:

$$\kappa_g I_b(T_g) = \max\left(\chi_r \dot{Q}_c''', \frac{\kappa_g \sigma_B T_g^4}{\pi}\right) \tag{10}$$

where χ_r (discussed further in the next section) is the fraction of the chemical heat release rate per unit volume, $\dot{Q}_c'''$, that is radiated to the local volume surrounding the flame region, κ_g (m^{-1}) is gas radiation coefficient and σ_B (W m^{-2} K^{-4}) is the Stefan-Boltzmann constant.

In the condensed phase model, the bulk density and specific heat have contributions from dry virgin vegetative fuel, char, ash, and moisture,

$$\rho_b = \rho_{b,dry} + \rho_{b,char} + \rho_{b,ash} + \rho_{b,H_2O} \tag{11}$$

$$c_{p,e} = \frac{\rho_{b,dry} c_{p,dry} + \rho_{b,char} c_{p,char} + \rho_{b,ash} c_{p,ash} + \rho_{b,H_2O} c_{p,H_2O}}{\rho_b} \tag{12}$$

where initially $\rho_{b,H_2o} = M\rho_b$ The specific heats in the equations above are c_{p,H_2O} 4190 J kg^{-1} K^{-1}, $c_{p,ash} = 1244(T_e/300)^{0.315}$ J kg^{-1} K^{-1} [26] and:

$$c_{p,char} = 420 + 2.09T_e + 6.85\text{x}10^{-4}T_e^2 \quad \text{J kg}^{-1}\,\text{K}^{-1} \quad ([27]) \tag{13}$$

$$c_{p,dry} = 10 + 3.7T_e \quad \text{J kg}^{-1}\,\text{K}^{-1} \quad ([28]) \tag{14}$$

The rate of change of total vegetative fuel mass is

$$\frac{d\rho_b}{dt} = -R_{H_2O} - (1 - \chi_{char})R_{pyr} - (1 - \chi_{ash})R_{char} \tag{15}$$

and the rate of change for the components of the vegetative mass are next detailed where $\dot{()}$ denotes $d()/dt$:

$$\dot{\rho}_{b,H_2O} = -R_{H_2O} \tag{16}$$

$$\dot{\rho}_{b,dry} = -R_{pyr} \tag{17}$$

$$\dot{\rho}_{b,char} = \chi_{char} R_{pyr} - R_{char} \tag{18}$$

$$\dot{\rho}_{b,ash} = \chi_{ash} R_{char} \tag{19}$$

Gaseous products created during the thermal degradation process are water vapor (during drying), fuel vapor (during pyrolysis), and CO_2 (during char oxidation). The source terms (kg m^{-3}s^{-1}) for these species are, respectively, R_{H_2O}, $(1 - \chi_{char})R_{pyr}$, and $\left(1 + \nu_{O_2,char} - \chi_{ash}\right)R_{char}$. In addition, the char oxidation process consumes oxygen in the gas phase at a rate of $-\nu_{O_2,char}R_{char}$.

3.3. Numerical Cases Set Up

For each experimental case we set up the corresponding numerical case. The same notation presented in Table 1, but preceded by the letter *n* (to refer to *numerical*), was used to designate the numerical cases. In all the numerical cases, the computational domain was limited to the furniture calorimeter (3 m × 3 m × 3.84 m). A more detailed discussion on the size of the domain used herein can be found in [29]. The numerical implementation of the furniture calorimeter considered the hood, the corresponding extraction system and the bench surface (Figure 3). The material properties associated with the hood were those of steel and for the bench surface those of autoclaved aerated concrete. The hood was built using multiple rectangular obstructions stairstepped in order to represent the inclination of the hood structure. The same procedure was used to implement the bench surface for the up-slope cases (Figure 3b). The gases extraction system was described using a fixed volume flow boundary condition. The volume flow was set to match the actual volume flow in the smoke exhaust duct.

Ignition was modeled by means of ignitor particles elements whose temperature was fixed at 1000°C. Ignitor particles properties were set equal to those of the corresponding fuel bed particles. Thus, they formed a porous arrangement of 4 cm wide, 1 m long and with the same height of the vegetation fuel bed, which was located in front of the fuel bed of vegetation. Ignition lasted 18 s, and all the particles simultaneously reached the set temperature. The dimensions of the surface occupied by the ignitor particles, and the duration of the ignition, were estimated according to the amount of ethanol and vegetation involved in the experimental ignition phase. Moreover, the necessary time for the simulated flow to reach a quasi-stationary regime within the hood was considered. Even though this time is not a critical parameter for experimental fires, it is necessary to take it into account during the numerical fires. For this reason, numerical ignition was delayed 60 s. For more details on the ignition modeling see [29].

Table 3 lists the main thermo-physical input parameters required by WFDS for both the gas-phase and the vegetation. Moreover, the source from where they have been obtained or the methodology used to determine them is also provided. Concerning gas-phase combustion, it was modeled in all the cases by a single-step complete global reaction, taking into account the results of the ultimate analysis for the elemental composition of pine needles ($C_xH_yO_z$). However, since the char formed during the thermal degradation of pine needles was assumed to consist of pure carbon and ash, the corresponding part of char carbon (χ_{char}) was deducted

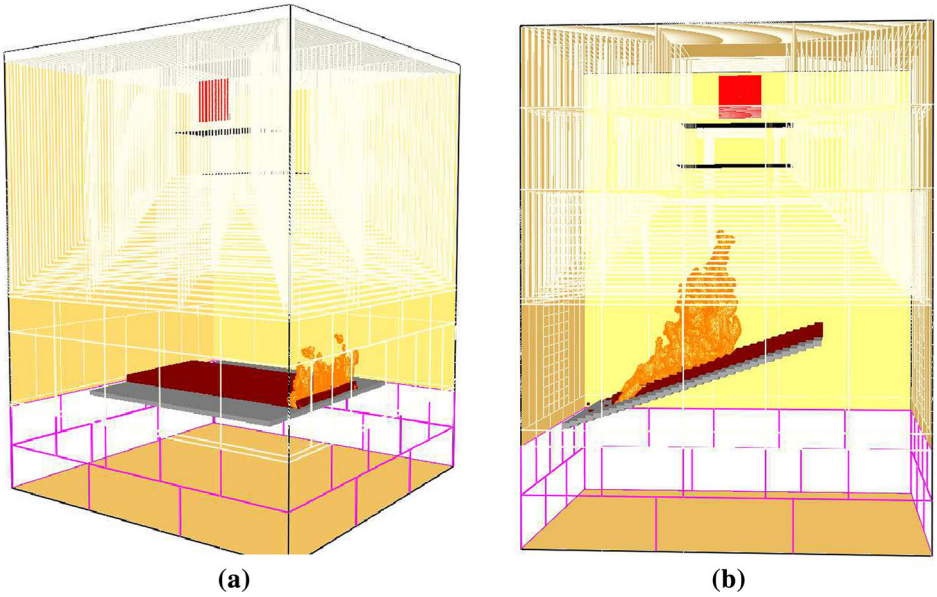

Figure 3. Numerical implementation of the LSHR apparatus as rendered by Smokeview (Version 6.1.4, Nov. 2013) [30]. (a) No-slope conditions (b) 20° up-slope conditions.

from the amount of carbon resulting from the elemental composition of pine needles. χ_{char}, the fraction of char formed during the thermal degradation of vegetation, was obtained from the literature [31] where χ_{char} of *Pinus pinaster* needles was measured by thermogravimetric analysis under inert atmosphere. In the same way, to obtain the mass-based heat of combustion of the gas-phase (Δh_c) we deducted from the value measured by using an oxygen bomb calorimeter, the fraction of energy released due to the char oxidation. This fraction of energy was computed as the product of the χ_{char} and the heat of combustion of char [24]. The fraction of local chemical heat release radiated to the surroundings (χ_r) was obtained experimentally. The methodology used and the values obtained are detailed in [10, 13]. The fraction of fuel consumed converted to soot (χ_s), was taken equal to 0.02 g/g according the literature [9]. The values considered for the ambient temperature (T_a) and the relative humidity (RH) where those measured during the experiments as reported in Table 3.

The vegetation parameters required by the particle-based WFDS fuel element model are as follows the surface-to-volume ratio (σ_e), the fuel particle density (ρ_e) and the drag coefficient factor (F_{C_D}), the bulk-density of the fuel bed (ρ_b), the depth of the fuel bed (h_b), the fuel moisture content (M), the fraction of char formed during the thermal degradation of vegetation (χ_{char}), the ash fraction formed during the oxidation of char (χ_{ash}) and the fraction of the energy produced by the char combustion reaction that is deposited in the solid phase (α_{char}). It is worth noting that for the numerical fuel bed depth the experimental values were

Table 3
Input Parameters Concerning Thermo-Physical Properties Required by the model

Phase	Symbol (units)	Value used	Comments
Gas	Δh_c (kJ kg^{-1})	16,360	Oxygen bomb calorimeter measurements following the standard AFNOR NF EN 14,918 corrected by deducting the corresponding energy fraction of char oxidation (Sect. 3.3)
	χ_r (−)	Experimental	No-slope cases: 0.17 (*n1_0*) – 0.20 (*n2_0*) – 0.22 (*n3_0*); Up-slope cases: 0.24 (*n1_20*, *n2_20*, *n3_20*) See detailed methodology in [10] [13],
	χ_s (−)	0.02	[9]
	T_a (°C)	Experimental	18°C – 24°C
	RH (%)	Experimental	26% – 50%
Solid	σ_e (m^{-1})	3057	Measured following the methodology proposed by Moro [32]
	ρ_e(kg m^{-3})	511	Measured following the methodology proposed by Moro [32]
	F_{C_D} (−)	0.375	[9]
	ρ_b(kg m^{-3})	Derived	See discussion in Sect. 3.3
	h_b (m)	Derived	Experimental values (Table 1) rounded, see discussion in Sect. 3.3
	M (-)	Experimental	No-slope cases: 0.05 (*n1_0, n2_0, n3_0*); Up-slope cases: 0.03 (*n1_20*) – 0.05, 0.08 (*n2_20*) – 0.08 (*n3_20*) (Section 3.3)
	χ_{char} (-)	0.27	[31]
	χ_{ash} (-)	Experimental	0.11
	α_{char} (-)	0.5	[21–23]

rounded in order to be consistent with the grid resolution of the mesh. This results in an integral number of grid cells spanning the height of the fuel bed. In order to keep the same amount of fuel in the experimental and numerical cases (fuel load, kg/m^2), we adjusted the values of the numerical bulk density according to the values of the numerical fuel bed depth. The mean differences between experimental and numerical bulk density were around 9.3%. Moreover, fuel moisture content (M) was obtained by averaging the measured values during the test replications of an experimental case. For the experimental case *2_20* measured values of fuel moisture content were either around 5% or 8%, so both values were considered (see Sect. 5.3, *Up-slope cases*). Concerning χ_{ash} it was measured during the experiments and a mean value was used for all numerical cases. Regarding α_{char} it was considered, according to the literature [21–23], that the energy released during the char oxidation was equally distributed into the gas and the solid phase.

Calculations were run in different HPC clusters: OCCIGEN at CINES (*Centre Informatique National de l'Enseignement Supérieur*, France), ROMEO at HPC Center of Champagne-Ardenne (France) and BRANDO at University of Corsica (France). The corresponding characteristics per node are next detailed. OCCIGEN: 2 × 12-core Intel Xeon Haswell processor, 2.6 GHz, shared memory. ROMEO: 2 × 8-core Intel Ivy Bridge processor, 2.6 GHz, 32 GB. BRANDO: 2 × 12-core Intel Xeon E5-2670V3 processor, 2.30 GHz, 64 GB. For the simulations demanding highest computing resources, 238 cores and a mean time of simulation of about 48 h were necessary. No differences, in terms of the obtained results, were observed when running the same case in the different clusters.

4. Sensitivity Analysis

4.1. Flow Within the Hood

The aim of this analysis was twofold: on the one hand to assess the suitability of the numerical implementation of the hood extraction system, and on the second hand to determine the more appropriate grid resolution for non-reacting flow simulations to be used in the parts of the domain located far from the combustion area. As previously mentioned, calorimetric calculations are based on the measurement of oxygen consumption. To this purpose, a hood extraction system collects the gases released from combustion. It is thus necessary to assess the capabilities of WFDS to reproduce the flow induced by the hood extraction system of the LSHR within the hood volume. This is a key step in order to ensure that the simulation results are independent of the features of the numerical representation of the LSHR. The grid size is an important numerical parameter that directly affects the calculation time and the simulation results. It is necessary to assess the influence of grid resolution on simulation results through a grid sensitivity study.

To that end, the experimental measurements of the airflow velocities within the hood were compared to the results of several simulations carried out using cubic cells of different sizes: 10.0, 5.0 and 2.5 cm. The airflow velocity magnitude, the v

velocity component (y-axis, Figure 2a) and w velocity component (z-axis, Figure 2a) of the simulated flow were recorded at different points in the computational domain corresponding to the same positions where experimental measurements were performed. The values recorded were instantaneous values which were then averaged over a 300 s period. In order to allow the numerical flow to reach a quasi-stationary regime within the hood the reading of the velocity values started 60 s after the beginning of the simulation.

The results obtained at the center of the bench for velocity magnitude are presented in Figure 4. In order to facilitate the reading of the results in this figure, only the standard deviations (std) associated to the hotwire anemometer measurements are illustrated. As it can be observed from 0.2 m up to 0.8 m there are no significant differences between the numerical results due to the grid size used. From 0.8 m up to 1.5 m differences between simulated velocities are getting larger, especially for the case of 10 cm grid size. It is thus clear that a grid resolution of 10 cm is not adequate to capture the flow dynamics in this area where the flow is more disturbed by the hood. Correspondingly a grid resolution of 5 cm seems a good compromise solution between calculation time and precision to simulate the airflow. But it is still necessary to verify that these values are in accordance with the measured ones. In this regard, if experimental measurements and predicted velocity magnitude values are compared, the same tendency can be observed from 0.2 m up to 0.8 m, but the values significantly differ. The average difference is about 0.14 m/s. From 0.8 m up to 1.5 m the values of the predicted velocity magnitude obtained for the grid resolutions of 2.5 cm and 5.0 cm are in agreement with the measured velocity values if the associated standard deviation is considered.

Figure 5 presents the v and w velocity components obtained for a grid resolution of 2.5 cm which have been plotted together with the experimental results.

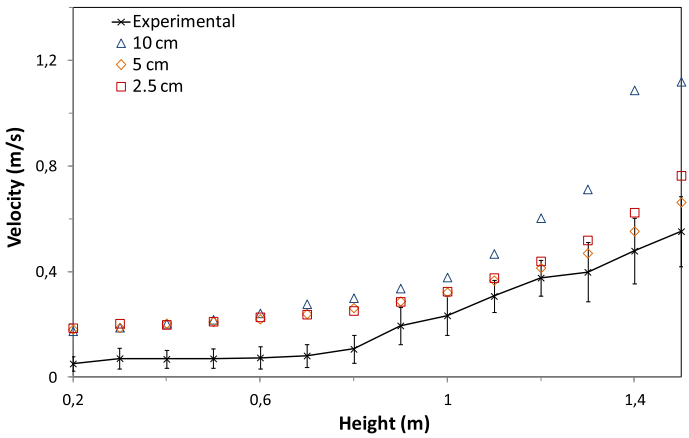

Figure 4. Time averaged simulated velocity magnitude and measured velocity along the vertical centerline in the hood versus height at position C.

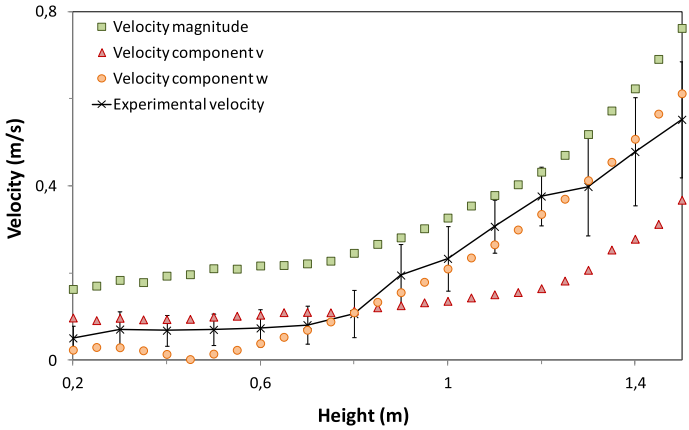

Figure 5. Time averaged simulated velocity components, simulated velocity magnitude and measured velocity along the vertical centerline in the hood versus height at position C.

These results show how velocities measured with the hotwire anemometer follow the trend of the prevailing simulated velocity component, v or w, with a turning point in the flow occurring at a height of approximately 0.8 m. Below 0.8 m the flow is parallel to the bench surface due to the suction effect induced by the hood. In this region the predominant velocity components are u (x-axis, Figure 2a) and v. Since the probe sensor was placed along the symmetry axis of the bench (x-axis, Figure 2a) and considering its characteristics, the anemometer mainly captures the velocity component v, as predicted by the model. As height increases, the flow becomes perpendicular to the suction intake, and thus the main velocity component is w, which is also consistent with the model predictions. From these results it can be concluded that for grid sizes up to 5 cm WFDS reproduces fairly well the flow velocities within the hood. The same conclusions can be derived from the comparison of the numerical simulations and the airflow measurements at point A (not shown).

Table 4
Characteristic Length Scales and the Associated Grid Cell Sizes

Experimental case	δ_R (m)	$dx_{b,\delta_R/3}$ (m)	$dx_{b,\delta_R/5}$ (m)	$z_{c,line}$ (m)	$dx_{g,z_c min}$(m)	$dx_{g,z_c max}$ (m)
1_0	0.041	0.014	0.008	0.111	0.007	0.028
2_0	0.043	0.014	0.009	0.184	0.012	0.046
3_0	0.038	0.013	0.008	0.241	0.015	0.060
1_20	0.040	0.013	0.008	0.159	0.010	0.040
2_20	0.043	0.014	0.009	0.230	0.014	0.058
3_20	0.044	0.015	0.009	0.284	0.018	0.071

4.2. Reacting Flow and Radiation Heat Transfer Within the Fuel Bed

This analysis was devoted to the determination of the sensitivity of the simulation results to grid resolution for the fire spread in the conditions of this study. Thus, different grid cell sizes were implemented for the simulation of the spreading fires within the LSHR in order to study the effect of grid size on the numerical HRR. The appropriate grid size depends on the characteristic length scales of the phenomena controlling fire spread. In order to obtain an initial estimate of the range of suitable values for this simulation, two different characteristic length scales were considered the first for the fuel bed and the second for the reacting flow. In plume-dominated fires, which are governed by radiation, the extinction length (δ_R) characterizing the absorption of radiation by vegetation has been identified in the literature [1] as the governing length scale in the vegetation fuel bed. δ_R can be obtained from the volume fraction of the solid-phase (α_e) and the surface-to-volume ratio of fuel particles (σ_e) as detailed below.

$$\delta_R = \frac{4}{\alpha_e \sigma_e} \tag{20}$$

The grid cell size used in the fuel bed (dx_b) has to be lower than δ_R. In this regard, Mell et al. [8] propose to used at most a grid cell size three times lower than δ_R ($dx_{b,\delta_R/3}$, Table 4), whereas Morvan and Dupuy [22] propose to use a grid cell size five times lower than δ_R ($dx_{b,\delta_R/5}$, Table 4).

Correspondingly, for flow field in buoyant plumes from pool fires McGrattan et al. [14] propose a length scale characterizing the diameter of the pool fire, z_c, defined by means of the heat release rate of the fire ($\dot{q}$) as follows:

$$z_c = \left(\frac{\dot{q}}{\rho_a c_{p,a} T_a \sqrt{g}}\right)^{2/5} \tag{21}$$

where ρ_a, c_p, T_a are respectively the density, specific heat and temperature of ambient air, and g is the standard gravity. In the experiments of this work, fire spreads forming a fire front line. The characteristic length scale for a line plume is given by [33]:

$$z_{c,line} = \left(\frac{\dot{q}'}{\rho_a c_{p,a} T_a \sqrt{g}}\right)^{2/3} \tag{22}$$

where $\dot{q}'$ corresponds to the fire line intensity, i.e. the energy release rate per unit length of the fire.

Mc Grattan et al. [14] suggest that the ratio between z_c and the grid cell size in the gas-phase (dx_g) has to range between 4 and 16. This criterion has been used to compute correspondingly $dx_{g,z_c max}$ and $dx_{g,z_c min}$ using $z_{c,line}$ instead of z_c.

Table 4 presents the obtained values of δ_R and $z_{c,line}$ for each experimental case, as well as, the subsequent grid sizes for the fuel bed ($dx_{b,\delta_R/3}$, $dx_{b,\delta_R/5}$) and the

reacting flow ($dx_{g,z_c min}$, $dx_{g,z_c max}$). It is important to note that the $z_{c,line}$ calculation has been based on the mean HRR during the stationary phase. For no-slope fires, since the fire front remained quasi-linear the fire line intensity is equivalent to the HRR. For up-slope fires, fire line intensity was determined by dividing the HRR by the fire front length during the stationary phase. Fire front length was obtained from image processing (for more details see [13]).

As it can be observed, according to the extinction length scale the grid cell sizes used within the fuel bed must be lower than 1.5 cm, or better, lower than 0.9 cm. Since δ_R depends on the fuel bed and particle characteristics and the volume fraction of the fuel bed is almost constant varying from 0.030 to 0.034, there are no significant differences between the experimental cases. On the contrary, since the grid cell size for the reacting flow derived from $z_{c,line}$ depends on the fire line intensity which was computed from the HRR, it greatly varied between experimental cases. The lower the fire line intensity the finer the necessary grid size.

Since for the same fuel load, no-slope cases present lower fire line intensity values than up-slope cases, only no-slope cases were considered in this analysis. Moreover, the same grid cell size for the combustion area (fuel bed and gas-phase) was considered given that the values obtained by computing $dx_{b,\delta_R/3}$ and $dx_{g,z_c min}$ were similar excepting for the case *1_0* where $dx_{g,z_c min}$ was closer to $dx_{b,\delta_R/5}$. Thus, for the numerical cases *n1_0*, *n2_0* and *n3_0* simulations were run with cubic cells of 3.0, 2.0, 1.5 and 1.0 cm size in the combustion area, in accordance with the grid sizes computed (Table 4) and the features of the computational resources. For computational time saving reasons coarser meshes were used far from the combustion area, except for the simulations run with a grid cell size of 3.0 cm. The grid cell size in these regions of the domain doubled the grid cell size in the combustion area, being consistent with the grid cell size value previously obtained to capture the flow dynamics within the hood (up to 5 cm).

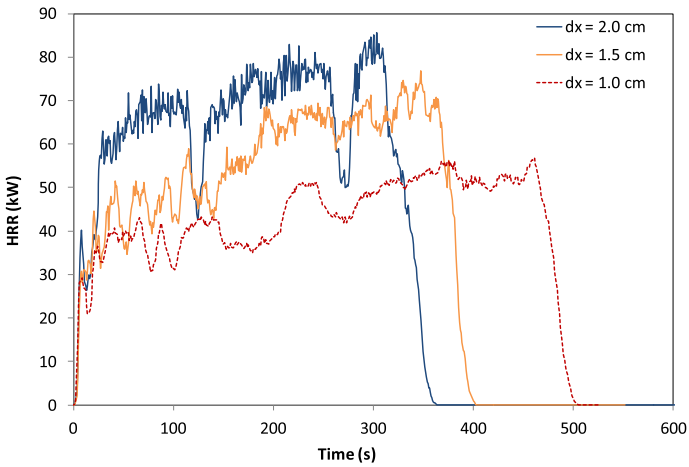

Figure 6. WFDS HRR for different grid sizes (dx) case n1_0 (0.6 kg/m2 no-slope).

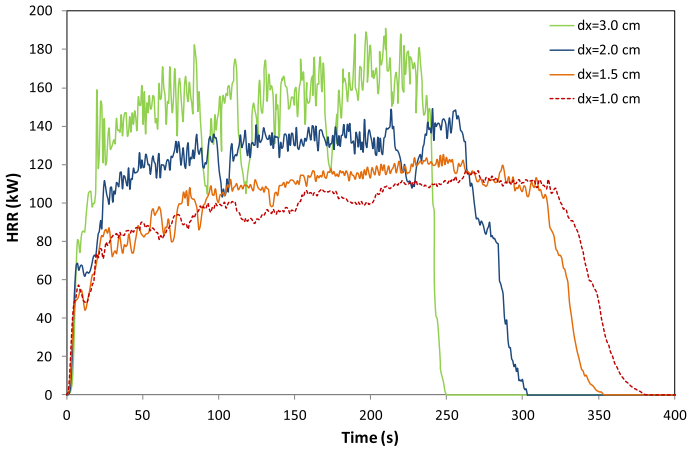

Figure 7. WFDS HRR for different grid sizes (dx) case n2_0 (0.9 kg/m2 no-slope).

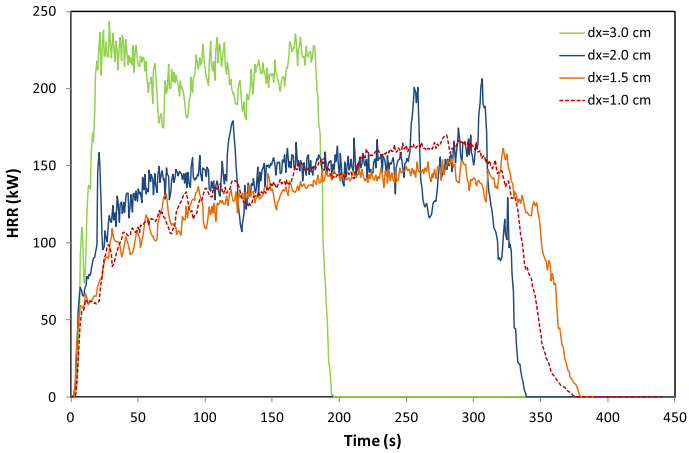

Figure 8. WFDS HRR for different grid sizes (dx) case n3_0 (1.2 kg/m2 no-slope).

Figures 6, 7 and 8 show respectively the numerical total HRR (gases and char, see Sect. 5.2) for the cases *n1_0*, *n2_0* and *n3_0*. It is worth noting that in the case *n1_0,* the results obtained by using a grid cell size of 3.0 cm have not been plotted in Figure 6 in order to facilitate the visualization of the results obtained with the other grid resolutions. According to the results presented in Figure 6 for the case *n1_0* it would be necessary to run simulations with grid resolutions lower than 1 cm to be sure that no significant modifications of HRR are observed for finer grid resolutions. However, reducing the grid size beyond 1 cm is computationally too expensive. This result was expected given the estimates of the necessary grid cell size (Table 4). On the contrary, for the cases *n2_0* and *n3_0* it can be observed

that the HRR curves tend to converge progressively as the grid resolution decreases. In both cases, slight differences on HRR between results obtained for grid resolutions of 1.5 cm and 1.0 cm can be explained by differences on the mesh configuration precisely due to the grid size. Thus, in the conditions of this study $dx_{g,z_c min}$ provides the best estimate of the grid size that allows non-grid dependent solutions. For the comparison of the experimental and numerical HRR a grid cell size of 1 cm was used for all the cases, even if greater values could have been used in certain cases according to these results.

5. HRR Results

5.1. Experimental HRR

In this section, experimental results of HRR are briefly presented to facilitate the subsequent analysis and comparison with the numerical results. As already specified, the instantaneous measures of HRR by OCC correspond both to the contribution of flaming combustion and char oxidation. After the ignition, the flame front develops and starts spreading across the fuel bed followed by a trailing smoldering/glowing front (i.e. surface just behind the fire front burning through heterogeneous reactions). The shape of both flaming and smoldering/glowing fronts is influenced by the effect of the slope which plays an important role in fire behavior. The instantaneous amount of fuel burning, and thus the derived HRR, depends on the shape and area covered by these fronts.

5.1.1. No-Slope Cases No-slope fires burnt at an almost constant rate of spread depending on the fuel load. The fire front exhibited a nearly linear shape, and it was followed by a smoldering/glowing front covering an almost constant surface area all along the duration of fire spread (Figure 9).

Figure 10 presents the instantaneous HRR measured obtained by averaging the replications of each experimental case. For each case, different stages can be

Figure 9. Image of a no-slope experimental test.

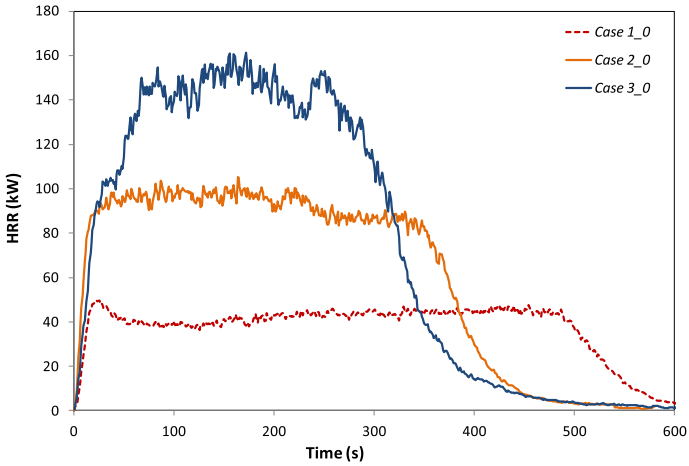

Figure 10. HRR versus time for no-slope experimental cases (mean values of the tests replicates).

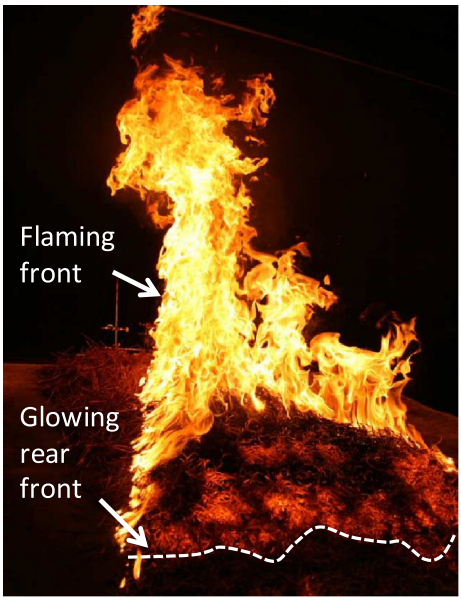

Figure 11. Image of an up-slope test.

clearly identified, the ignition distinguished by the rapid increase of HRR, a steady-state phase where HRR is almost constant and finally the extinction phase characterized by a gradual decrease of HRR.

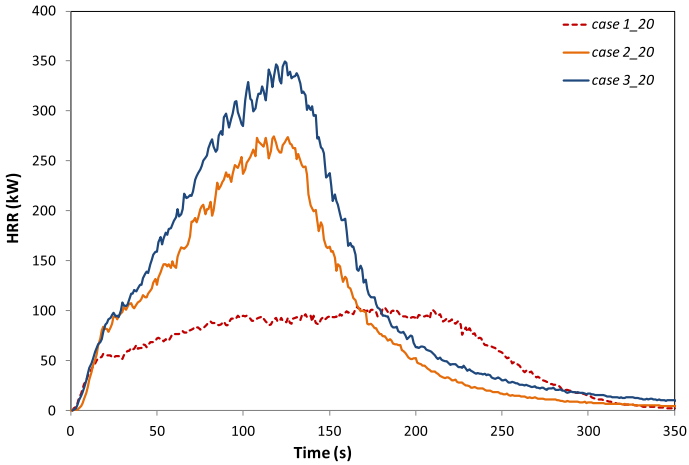

Figure 12. HRR versus time for up-slope experimental cases (mean values of the tests replicates).

5.1.2. Up-Slope Cases The flame front of up-slope fires was not linear. As the fire develops, the fire front distorts since it spreads faster at the center than at the edges, getting thus an inverted-V shape (Figure 11). This distortion is intensified by increasing the fuel load. As flame front advances, the surface covered by the glowing/smoldering front increases because the combustion in the solid-phase is slower than the flaming combustion at the head of the fire perimeter. The glowing/smoldering front shape is thus modified in comparison with no-slope fires, and the area covered increases over time. Accordingly HRR increases over time until it reaches a stationary phase, whose duration strongly decreases with fuel load as illustrated in Figure 12. Moreover, the duration of the stationary phase is also dependant on the fuel moisture content of vegetation, the lower the fuel moisture content the shorter the stationary phase. As for no-slope cases, different stages can be clearly identified from the HRR curves, the ignition, then a growing phase characterized by the fast increase in HRR, a short stationary phase and the extinction phase where flaming combustion has ended and only char oxidation persists. As for no-slope fires, during the extinction phase a gradual decrease of HRR can be observed.

5.2. Numerical HRR

WFDS computes separately the HRR due to the gas-phase reactions and the HRR due to solid-phase oxidation reactions. Since the instantaneous measures of HRR obtained by OCC correspond to the contribution of both gas and solid phase reactions, henceforth the term HRR (or total HRR) refers here to the energy released by the fire during flaming and glowing/smoldering combustion. Correspondingly, gas HRR refers to the energy released only due to the gas-phase reactions and char HRR to the energy released only due to solid-phase oxidation reactions.

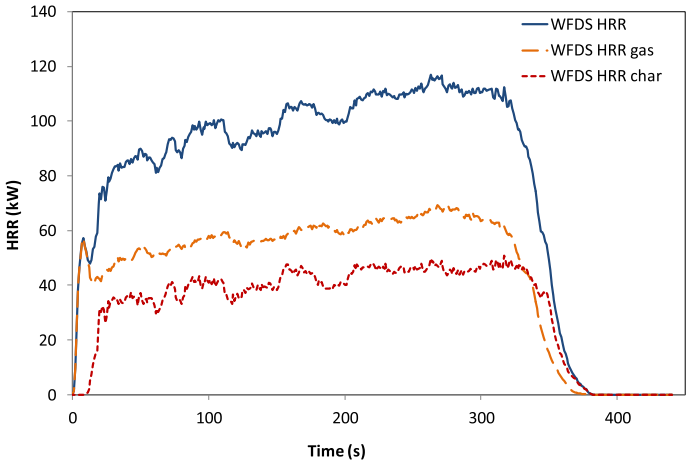

Figure 13. Numerical HRR, gas HRR and char HRR for the case n2_0.

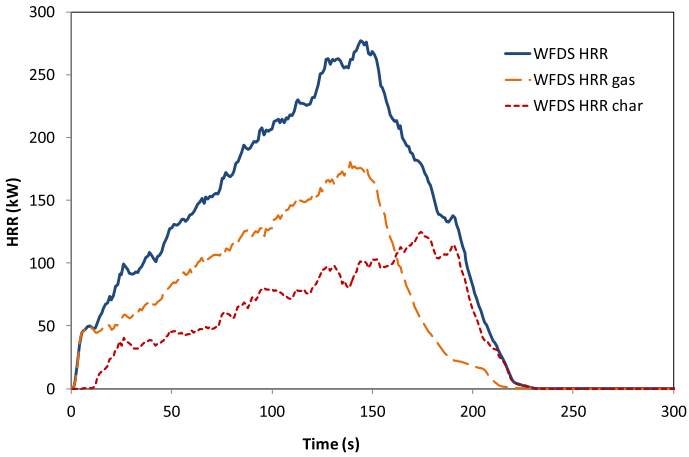

Figure 14. Numerical HRR, gas HRR and char HRR for the case n2_20, M = 8%.

Figure 13 shows the results of the instantaneous HRR, gas HRR and char HRR for the numerical case *n2_0* which is representative of the results of all the no-slope cases. As it can be observed, char oxidation starts after the ignition of the fuel bed, around 12 s later for this particular case, 17 s for the numerical case *n3_0* and 8 s for the numerical case *n1_0*. These values are in agreement with the observed residence time of the flame front. The curves of gas HRR and char HRR follow the same tendency, indicating that the surface involved in combustion processes is almost constant over time which is consistent with the observed experimental behavior. The contribution of gas HRR to the total HRR during the steady-state phase accounts for 60%, correspondingly the contribution of char

HRR is about 40%. The important contribution of char HRR to the total HRR can be explained by both the mass of dry fuel which is converted to char and follows heterogeneous solid-phase reactions; and the highly exothermic character of these reactions in comparison to the gas-phase combustion reactions.

In the case of up-slope numerical fires, Figure 14 presents the results for the particular case *n2_20*. In this case, total HRR, gas HRR and char HRR increase over time till the extinction phase when subsequently flaming combustion and char combustion cease. This increase over time implies that the amount of vegetation involved in combustion processes also increases, as does the surface area covered by the fire. The shape of the numerical curves of HRR is in agreement with the experimental observations. The same tendency is observed for the other up-slope cases.

5.3. Measured and Predicted HRR

Numerical results of HRR (i.e. gas HRR plus char HRR) obtained with the higher grid resolution, i.e. 1 cm, have been compared to the experimental results of HRR. A detailed analysis of the results of the experiments carried out including HRR among other parameters can be found in [10, 13]. However, concerning HRR results, only mean and peak HRR values are presented in these publications as well as some examples of experimental curves. Here, and in order to facilitate the analysis we have computed the mean value of instantaneous HRR over time of the different replications for each experimental case as well as the standard deviation (std). Figure 15a, b show, respectively, the HRR results for all the replications of the experimental case *1_0* and the mean HRR with the associated standard deviation. As it can be seen on these figures, the mean HRR curve is not representative of the large-scale fluctuations observed experimentally. In fact, this mean value, associated with the corresponding standard deviation, is intended to represent here the range of the possible values of HRR for a particular experimental case.

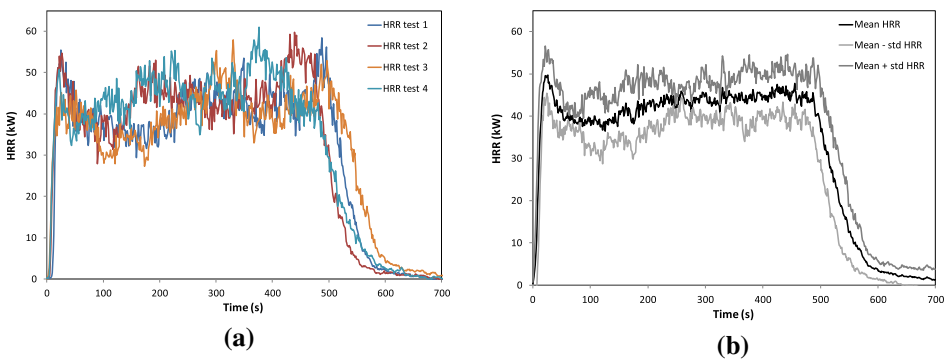

Figure 15. Results for the case 1_0 experiments. (a) Instantaneous HRR of the different replications (b) Mean HRR with the associated standard deviation.

5.3.1. No-Slope Cases Figure 16 shows both the experimental and the simulated HRR results versus time for each of the three no-slope experimental cases. On the left side of Figure 16, the mean and standard deviation of the measured HRR are plotted along with the simulated HRR. On the right side of Figure 16, the single replicate experiment that best matches the simulated HRR is plotted. In a general way, numerical HRR during the steady state is in quite good agreement with the range of the expected values of experimental HRR. This is confirmed by the comparison of numerical HRR with the best matching experimental curve of HRR. Moreover, the duration of the combustion, which is related to the rate of spread is correctly predicted. A slight increasing trend in the numerical HRR is observed for all the cases. This trend is also observed experimentally in certain cases, either when some of the needles at the edge of the fuel bed do not burn completely or due to the cooling effect of air entrainment at the edge of the fuel bed which produces a slight deformation of the fire front in this area, increasing the perimeter of the fire and thus the HRR. Also, a difference can be observed during the extinction phase where the predicted HRR decreases more rapidly than the experimental HRR. If the particular case and experimental test presented in Figure 16b are considered, the difference between the actual amount of energy released during the experimental extinction phase and the numerical one is lower than 6.5% of the total amount of energy released during the fire test (test 4 replicate of case *1_0*). Considering this further, Figure 17 illustrates the instantaneous difference between actual and numerical HRR (ΔHRR) for this case and the test 4 replicate of case *1_0*, where the black area corresponds to the difference in the energy released during the extinction phase. If the total energy released by the numerical fire and the fire test are compared, the absolute difference observed is lower than 18.5%. For the cases n*2_0* and *n3_0* and the experimental tests presented in Figure 16d and f the difference between the actual and the numerical amount of energy released during the extinction phase in terms of the total amount of energy released during the fire test are respectively 5.4% and 5.5%. Concerning the absolute difference between the numerical and the actual total energy released, the values are 18.6% and 16.7%, respectively. If the difference between numerical and experimental values is considered only when numerical values fall out of the interval (Mean—std HRR, Mean + std HRR) of experimental values, then the absolute difference between numerical and experimental values (mean—std HRR if the model under predict HRR or mean + std if the model over predict HRR) corresponds to the 8% of the mean total energy released for the case *1_0*. The corresponding values for the cases *2_0* and *3_0* are 11.8% and 6.2%.

HRR is strongly linked to the solid-phase degradation model. Since MLR is the result of both gas release and char formation and oxidation, it can be considered as a relevant quantity to compare simulated results and experimental observations. For this reason, the predicted MLR values have also been considered herein to give a deeper insight into the capabilities of WFDS to predict fire behavior. Figure 18 presents the coupled results of HRR and MLR of numerical case *n3_0* and the best matching experimental test (test 3 replicate of case *3_0*). As observed in this figure, once the numerical combustion ceases (numerical MLR is equal to zero), there are still some char oxidation reactions going on in the experimental

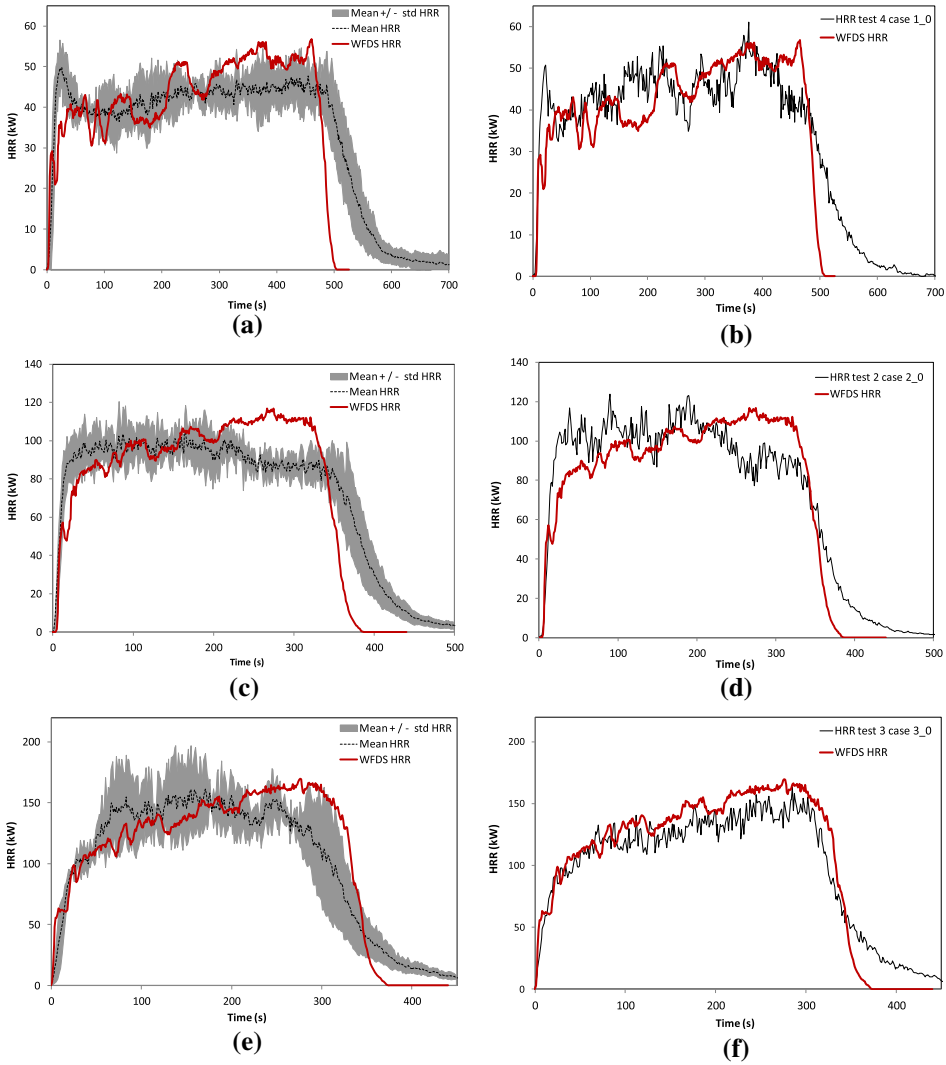

Figure 16. Experimental and numerical HRR for no-slope cases. Mean and standard deviation of the measured HRR versus time (*left*), and the best matching experimental HRR (*right*) (a) case n1_0 and case 1_0 (b) case n1_0 and test 4 replicate of case 1_0, (c) case n2_0 and case 2_0 (d) case n2_0 and test 2 replicate of case 2_0, (e) case n3_0 and case 3_0 (f) case n3_0 and test 3 replicate of case 3_0.

test according to visual observations. During the extinction phase, experimental MLR values decrease monotonically but with large, short duration, fluctuations. The largest differences between numerical and experimental MLR in this phase are about 2 g/s. Since the char oxidation reactions are highly exothermic, underestimation of the predicted MLR of 2 g/s can result in an error of about 60 kW in

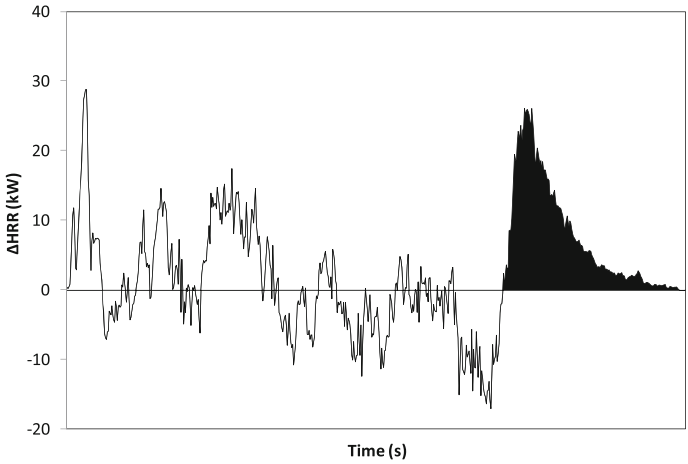

Figure 17. Instantaneous differences between experimental HRR test 4 replicate of case 1_0 and numerical HRR. *Black colored area* corresponds to the extinction phase.

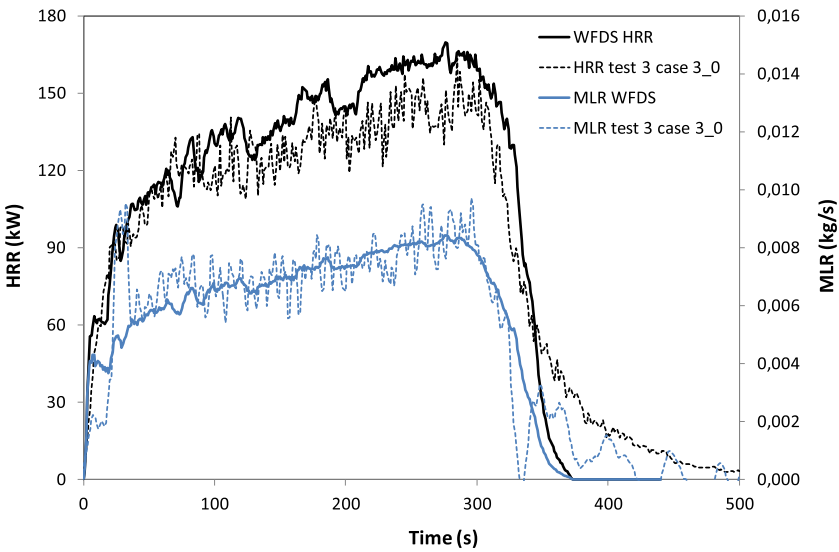

Figure 18. HRR and MLR case n3_0, experimental HRR and MLR test 3 replicate of case 3_0 versus time.

the prediction of instantaneous HRR. It is worth noting that at this stage we near the limit of the load cell measurement capability (1 g/s).

The same behavior during the extinction phase in terms of MLR is also reproduced for the rest of numerical cases. In this regard, Figure 19 shows the results of HRR and MLR of the numerical case *n2_0* and the corresponding best match-

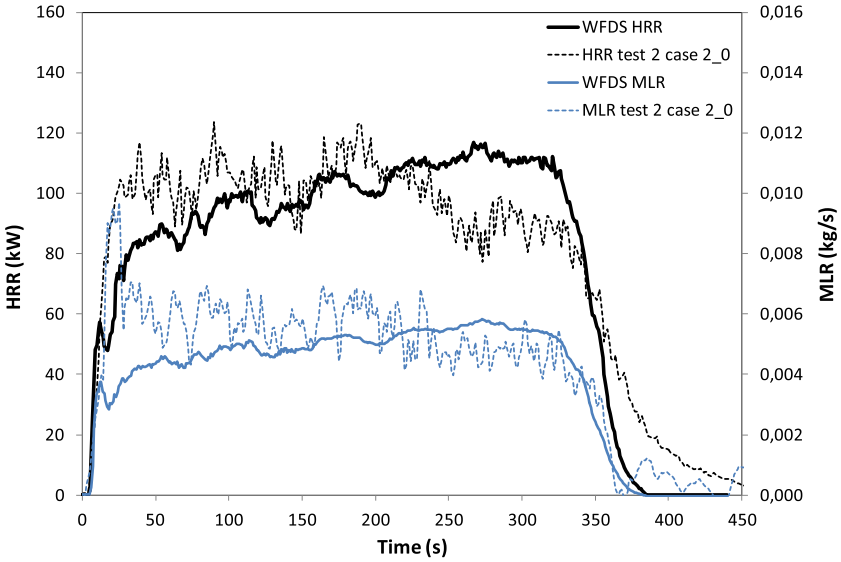

Figure 19. HRR and MLR case n2_0, experimental HRR and MLR test 2 replicate of case 2_0 versus time.

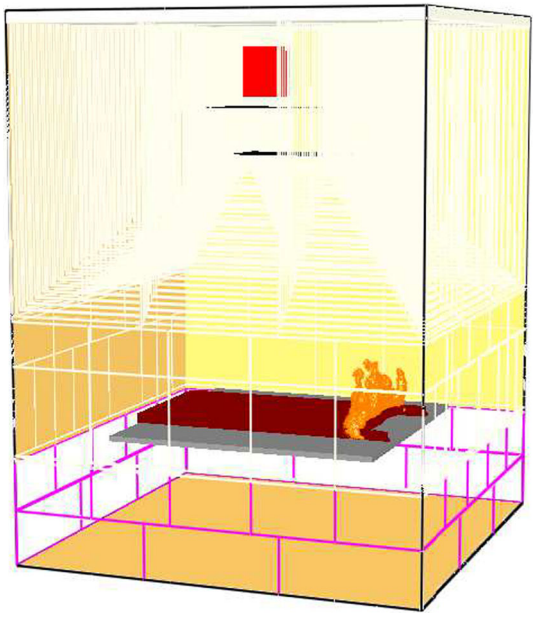

Figure 20. Fire spread during the numerical case n2_0 as rendered by Smokeview. Unconsumed vegetation can be seen along the side of the fuel bed.

ing experimental test (test 2 replicate of case *2_0*). Moreover, in this particular case a different behavior is observed during fire spread with an increasing trend in HRR at the first stage of fire spread (Figure 16d). This tendency is confirmed by MLR results, indicating that a lower amount of vegetation is burning in the numerical case than in the experimental test from the ignition up to 100 s. Indeed, when analyzing the predicted mass consumption it is found that not all the numerical vegetation particles burn. The visualization of numerical results by means of the package Smokeview shows that unburned particles are located at the edge of the fuel bed (Figure 20). As previously stated, this behavior has also been observed in other experimental cases.

5.3.2. Up-Slope Cases As for no-slope cases, Figure 21 shows both the experimental and the simulated HRR results versus time for each of the three 20° up-slope experimental cases. On the left side of Figure 21, the mean and standard deviation of the measured HRR are plotted along with the simulated HRR. On the right side of Figure 21, the single replicate experiment that best matches the simulated HRR is plotted. For the case *n1_20*, WFDS reproduces remarkably well the measured HRR including the extinction phase. The absolute difference between numerical and experimental values (mean—std HRR if the model under predict HRR or mean + std if the model over predict HRR, Figure 21a) corresponds to the 4.6% of the mean total energy released for the case *1_20*. When comparing the predicted values of case *n1_20* with the test 3 replicate results (Figure 21b) then the absolute difference between the predicted and the actual energy released by the fire is lower than 13.6%. Concerning the case *n2_20*, the predicted results are in good agreement with the experimental observations. As illustrated in Figure 21c), the variability of experimental results is larger in this case than in the other two up-slope experimental cases. This is due to the fuel moisture content of vegetation, which significantly varied between the different replication tests. For this reason, two different values of fuel moisture content were used in the simulations, 5% (Figure 21c and d, Figure22a) and 8% (Figure 22b). As shown in Figure 22, WFDS correctly predicts the effect of fuel moisture content in HRR for the values considered in this study. It is worth noting that for the test replicate 1 (Figure 22b) the fuel moisture content was around 9%, and for the test replicate 4, it was 7.5% (Figure 22b). These differences between experimental and numerical fuel moisture content explain the best agreement between the numerical HRR and the measured HRR during test replicate 4 in comparison with test replicate 1. In this regard the absolute difference of the energy released by the numerical fire and the best matching test replicate is of the order of 19% no matter what fuel moisture content is considered.

For these two up-slope cases *n1_20* and *n2_20*, MLR predictions are also in good agreement with the measured values as illustrated in Figure 23 for the case *n2_20* (M = 8%). As previously observed for no-slope cases, the major differences observed between numerical and experimental MLR during the extinction phase are lower than 2 g/s.

Regarding the results for the up-slope case *n3_20* (Figure 21e and f), the predicted HRR increases monotonically to reach a peak value close to 500 kW,

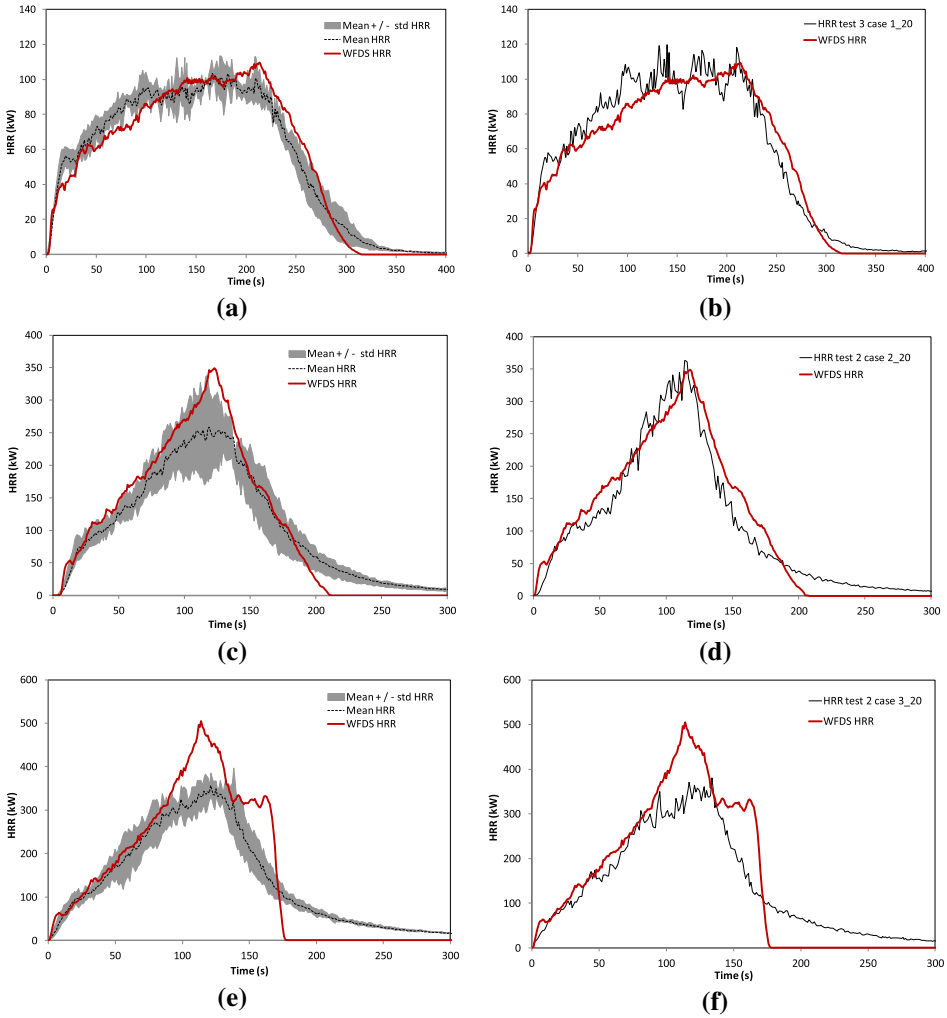

Figure 21. Experimental and numerical HRR for 20° up-slope cases. Mean and standard deviation of the measured HRR versus time (*left*), and the best matching experimental HRR (*right*) (a) case n1_20 and case 1_20 (b) case n1_20 and test 3 replicate of case 1_20, (c) case n2_20 (M = 5%) and case 2_20 (d) case n2_20 (M = 5%) and test 2 replicate of case 2_20, (e) case n3_20 and case 3_20 (f) case n3_20 and test 2 replicate of case 3_20.

whereas experimental HRR during the steady state is around 350 kW. Moreover, important differences are also observed during the extinction phase. Figure 24 shows the predicted HRR and MLR as well as the corresponding experimental results for the test 2 replicate of case *3_20*. As it can be observed, numerical MLR follows the same trend as HRR. Indeed, numerical fire spreads faster than the

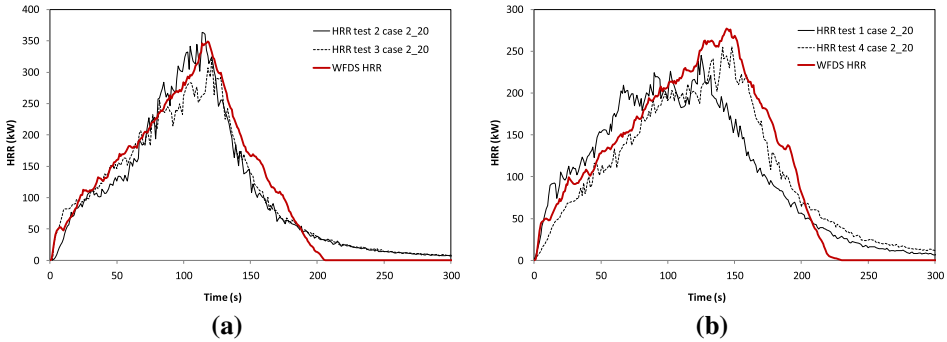

Figure 22. HRR results case n2_20 (0.9 kg/m2 – 20° slope) for different fuel moisture contents. (a) Numerical HRR and the two best experimental HRR matching M = 5%. (b) Numerical HRR and the two best experimental HRR matching M = 8%.

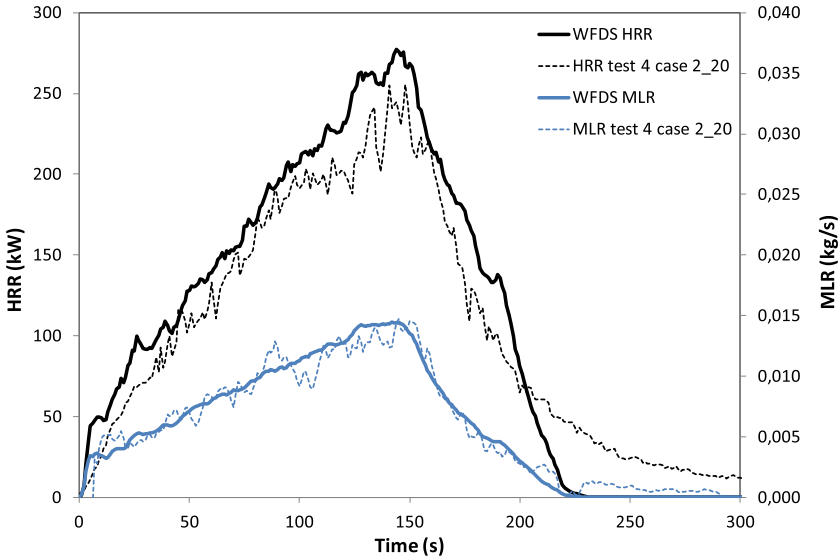

Figure 23. HRR and MLR case n2_20 M = 8%, experimental HRR and MLR test 4 replicate of case 2_20 versus time.

experimental fire, so the flaming front reaches the end of the experimental bench earlier of what is expected. As a result, the surface just behind the fire front involving solid-phase reactions is larger than in experimental fires, as well as the amount of vegetation instantaneously burning. Figure 25 presents the predicted HRR (total) and the corresponding gas HRR and char HRR. Concerning the HRR of the gas-phase reactions (*WFDS gas HRR*), a change in the slope of the curve is observed around 100 s. This instant coincides with the moment when the flames get in contact with the hood, according to the visualization of the numeri-

cal results by means of the package Smokeview. In fact, due to the size of the flames and the inclination of the bench, the flames impact the hood surface as also observed during the experiments. If the actual numerical radiative fraction is calculated as the ratio between the predicted integration of radiative HRR over the entire simulation domain (corresponding to *Q_RADI* output quantity of the model [14]) and the predicted HRR, an increasing tendency can be observed starting from 100 s after the ignition (Figure 26). This can result from the warning up of the surface of the hood inducing to numerical errors in the transport of the radiation. It is worth noting that for all the other cases the computed radiative fraction reaches a stationary value which is consistent with the input value. Concerning the HRR due to solid-phase combustion (*WFDS HRR char* in Figure 25), a change in the slope of the curve is observed 150 s after the ignition. At this moment, according to the visualization of the results with Smokeview, the flames front has already reached the end of the bench and flames start to extinguish intermittently while another char oxidation front appears at the end of the bench advancing backwards. This front is responsible for the sudden increase in the char HRR. Even if during the experiments we observed a similar behavior, the char oxidation was much slower. In order to study the effect of the numerical representation of the interaction between the flames and the hood on the predictions of HRR, a simulation was run for this case without the hood. The results show that the actual numerical radiative fraction it is almost constant (Figure 27). Moreover both gas and char HRR curves increase monotonically, however, during the extinction phase HRR decreases as rapidly as when the hood is present (not shown).

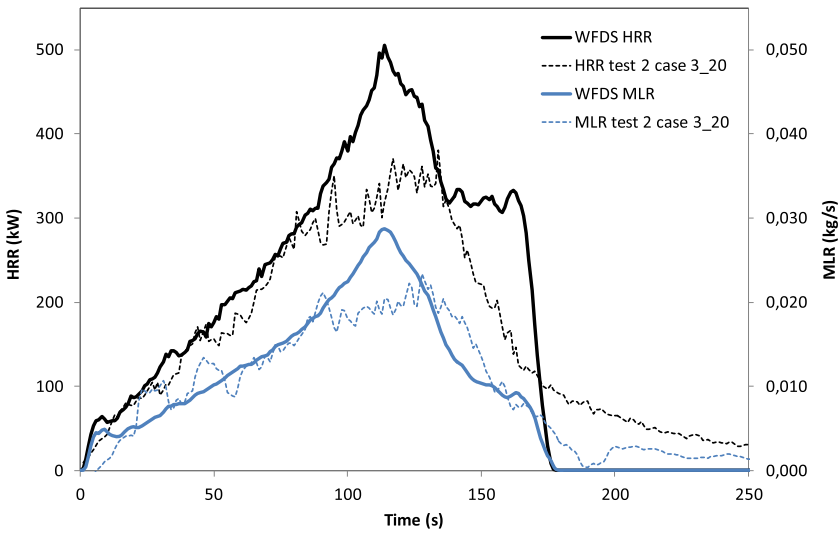

Figure 24. HRR and MLR case n3_20, experimental HRR and MLR test 2 replicate of case 3_20 versus time.

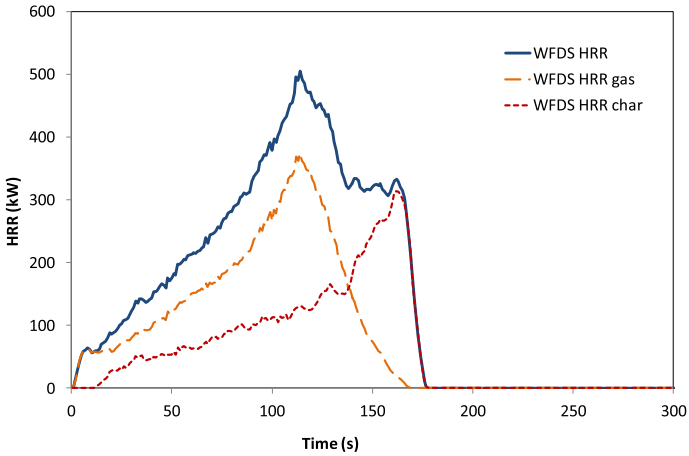

Figure 25. Predicted HRR (gas + char), gas HRR and char HRR for the case n3_20.

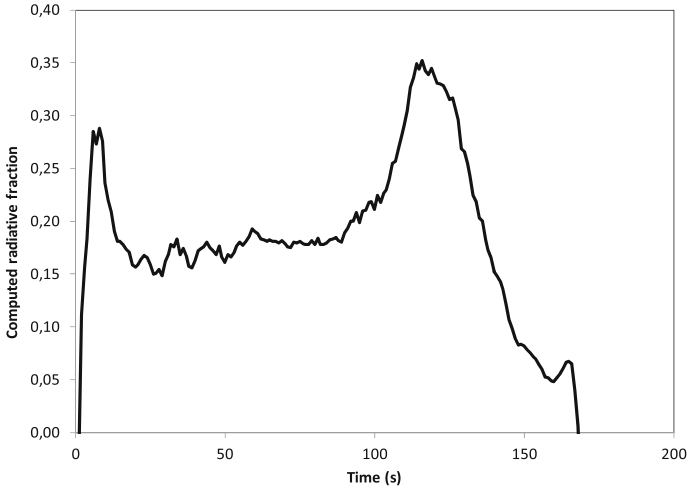

Figure 26. Computed radiative fraction for the case n3_20.

WFDS has predicted fairly well the instantaneous HRR for all the studied cases excepted for the case *3_20*. The main divergences have been observed during the extinction phase. The study of the MLR has shown that WFDS underpredicts the MLR during the char oxidation after the flameout. Even if the differences between predicted and observed MLR are small (about 2 g/s) the char oxidation reactions are highly exothermic producing observable differences in HRR. Houssami et al. [23] used a very similar solid-phase degradation model to simulate laboratory experiments carried out with porous pine needles beds in a FPA apparatus using samples between 6.4 g and 15 g. They observed according to the predicted results

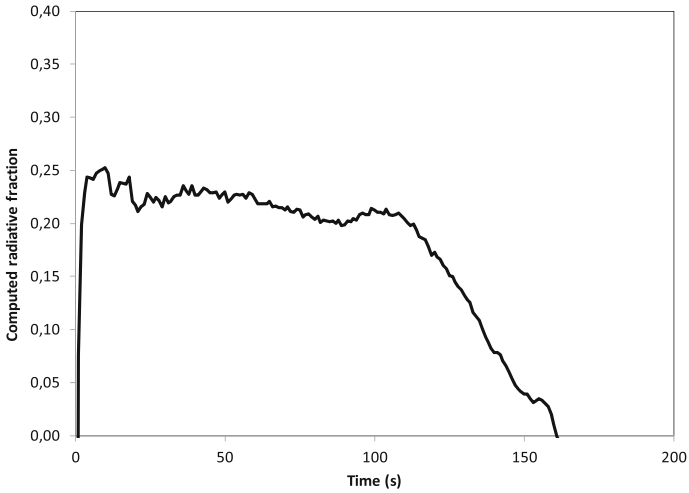

Figure 27. Computed radiative fraction for the case n3_20 without the hood.

that char oxidation rate was not sustained after flame out and concluded that a single step model does not able to represent the studied phenomenon.

6. Conclusions

For the first time WFDS including an Arrhenius type model for the solid-phase thermal degradation has been tested against instantaneous measurements of HRR by oxygen consumption calorimetry for no-slope and up-slope spreading fires at laboratory scale. In the first part of this work we have studied the accuracy of WFDS to represent the flow within the hood of the experimental device. Results have shown a good agreement between measured and simulated velocity profiles at different positions within the hood for grid resolutions lower than 5 cm. Moreover, a grid sensitivity analysis for reacting flows as well as the radiation heat transfer within in the fuel bed has been conducted in order to assess the grid resolution's influence on the outputs of the model. A grid resolution of 1 cm seems to be adequate for almost all the cases. A criterion based on the characteristic length scale of a fire line that gives the best estimate of the appropriate grid size cell in the combustion area has been identified. In the second part of this work, simulated and experimental instantaneous HRR have been compared. For no-slope cases, numerical HRR values are in reasonably good agreement with the range of experimental HRR data during the ignition phase and the steady-state of fire propagation. Moreover, WFDS correctly reproduces the duration of the flaming combustion phase, which is directly tied to the fire rate of spread. Concerning the extinction phase, char oxidation is faster for the simulated fires than for the experimental fires resulting in a more rapid decrease of HRR after the flameout. The analysis of MLR has shown that during the extinction phase, the predicted MLR

is underestimated. In the worst case, the observed difference between the actual and the predicted MLR is about 2 g/s. For up-slope cases, instantaneous HRR and MLR predictions of WFDS are in good agreement with experimental data for the cases *1_20* and *2_20*. However, for the higher fuel load corresponding to the experimental case *3_20*, the interaction between the flames and the hood is responsible for a higher rate spread for the numerical fire than observed in the experimental tests. As a result, the predicted instantaneous HRR reaches a peak value which is higher than the HRR measured. As for no-slope cases, char oxidation is faster for simulated fires than for experimental tests, especially in the case *n3_20*. WFDS has also proved to correctly predict the effect of fuel moisture content on the HRR, for values ranging between 3% and 8%. Future work will be focused on improving the char oxidation model. In addition, WFDS will be tested in other experimental conditions and against other important parameters for fire behavior characterization such as radiant heat flux and smoke.

Acknowledgments

This work was partly supported by the HPC Center of Champagne-Ardenne ROMEO, CINES (Centre Informatique National de l'Enseignement Supérieur) and the University of Corsica.

References

1. Morvan D (2011) Physical phenomena and length scales governing the behaviour of wildfires: a case for physical modelling. Fire Technol 47:437–460
2. Alexander M, Cruz MG (2013) Are the applications of wildland fire behavior models getting ahead of the evaluation again?. Environ Modell Softw 41:65–71
3. Babrauskas V, Peacock RD (1992) Heat release rate: the single most important variable in fire hasard. Fire Saf J 18:225–292
4. Fites JA, Henson C (2004) Real-time evaluation of effects of fuel treatments and other previous land management activities on fire behavior during wildfires. Report of the Joint fires science rapid response project. US Forest Service, pp 1–13
5. McAthur AG (1962) Control burning in eucalypt forests. Comm. Aust. For. Timb. Bur. Leafl. No. 80
6. Hammil KA, Bradstock RA (2006) Remote sensing of fire severity in Blue Mountains: influence of vegetation type and inferring fire intensity. Int J Wildland Fire 15:213–226
7. Sullivan AL, Ball R (2012) Thermal decomposition and combustion chemistry of cellulosic biomass. Atmos Environ 47:133–141
8. Mell WE, Jenkins MA, Gould J, Cheney P (2007) A physics-based approach to modelling grassland fires. Int J Wildland 16:1–22
9. Mell WE, Maranghides A, McDermott R, Manzello S (2009) Numerical simulation and experiments of burning Douglas fir trees. Combust Flame 156:2023–2041
10. Morandini F, Pérez-Ramirez Y, Tihay V, Santoni PA, Barboni T (2013) Global heat release, radiant and convective characterization of fires spreading across forest beds of fuel. Int J Therm Sci 70:83–91

11. Santoni PA, Morandini F, Barboni T (2011) Determination of fireline intensity by oxygen consumption calorimetry. J Therm Anal Calorim 104:1005–1015
12. Parker WJ (1982) Calculations of the heat release rate by oxygen consumption for various applications. NBSIR 81–2427–1
13. Tihay V, Morandini F, Santoni PA, Pérez-Ramirez Y, Barboni T (2014) Combustion of forest fuel beds under slope conditions: burning rate, heat release rate, convective and radiant fractions for different loads. Combust Flame 161(12):3237–3248
14. McGrattan K, Hostikka S, McDermott R, Floyd J, Weinschenk C, Overholt K (2013) Fire Dynamics Simulator User's Guide. Technical Report NIST Special Publication, 1019-6, National Institute of Standards and Technology, Gaithersburg, Maryland
15. Overholt KJ, Kurzawski AJ, Cabrera J, Koopersmith M, Ezekoye OA (2014) Fire behavior and heat fluxes for lab-scale burning of little bluestem grass. Fire Saf J 67:70–81
16. Overholt KJ, Cabrera J, Kurzawski A, Koopersmith M, Ezekoye OA (2014) Characterization of fuel properties and fire spread rates for little bluestem grass. Fire Technol 50(1):9–38
17. Castle D (2015) Numerical modeling of laboratory-scale surface-to-crown fire transition. M.S. Thesis, San Diego State University, California, USA
18. Mueller E, Mell W, Simeoni A (2014) Large eddy simulation of forest canopy flow for wildland fire modeling. Can J For Res 44:1534–1544
19. Buffachi P, Krieger GC, Mell W, Alvarado E, Santos JE, Carvalho JA (2016) Numerical simulation of surface fires in Brazilian Amazon. Fire Saf J 79:44–56
20. Hoffman CM, Canfield J, Linn RR, Mell W, Sieg CH, Pimont F, Ziegler J (2016) Evaluating crown fire rate of spread predictions from physics-based models. Fire Technol 52(1):221–237
21. Porterie B, Consalvi JL, Kaiss A, Loraud JC (2005) Predicting wildland fire behavior and emissions using a fine-scale physical model. Numer Heat Transf A Appl 47:571–591
22. Morvan D, Dupuy JL (2001) Modeling of fire spread through a forest fuel bed using a multiphase formulation. Combust Flame 127:1981–1994
23. El Houssami M, Thomas JC, Lamorlette A, Morvan D, Chaos M, Hadden R, Simeoni A (2016) Experimental and numerical studies characterizing the burning dynamics of wildland fuels. Combust Flame 168:113–126
24. Dahale A, Ferguson S, Shotorban B, Mahalingam S (2013) Effects of distribution of bulk density and moisture content on shrub fires. Int J Wildland Fire 22:625–641
25. Porterie B, Morvan D, Larini M, Loraud JC (1998) Wildfire propagation: a two dimensional multiphase approach. Combust Explos Shock Waves 34(1):139–150
26. Lautenberger C, Fernandez-Pello C (2009) A model for the oxidative pyrolysis of wood. Combust Flame 156:1503–1513
27. Park WC, Atreya A, Baum HR (2010) Experimental and theoretical investigation of heat and mass transfer processes during wood pyrolysis. Combust Flame 157(3):481–494
28. Ritchie SJ, Steckler KD, Hamins A, Cleary TG, Yang JC, Kashiwagi T (1997) The effect of sample size on the heat release rate of charring materials. Fire Saf Sci 5:177–188
29. Pérez-Ramirez Y, Santoni PA, Tramoni JB, Mell WE (2014) Numerical simulations of spreading fires in a large-scale calorimeter: The influence of the experimental configuration. In Viegas DX (Ed): Proceedings of the VII International Conference on Forest Fires Research

30. Forney GP (2012) Smokeview (Version 6)—A Tool for Visualizing Fire Dynamics Simulation Data. Volume I: User's Guide. NIST Special Publication 1017-1. National Institute of Standards and Technology, Gaithersburg, Maryland
31. Zaida TJ (2012) Etude expérimentale et numérique de la dégradation thermique des lits combustibles végétaux. PhD Thesis. University of Oaugadougou—Université de Poitiers (Laboratoire de Physique Chimie et de l'Environnement)
32. Moro C (2006) Détermination des caractéristiques physique de particules de quelques espèces forestières méditerranéennes, INRA PIF2006-06
33. Quintiere JG, Grove BS (1998) A unified analysis for fire plumes. In: Twenty Seventh Symposium (International) on Combustion. The Combustion Institute 2757–2766